Investigation of Eccentric PM on High-frequency Vibration in FSCW PM Machine Considering Force Modulation Effect*

Jinghua Ji, Weizhi Jiang, Wenxiang Zhao and *Tong Liu*

(School of Electrical and Information Engineering, Jiangsu University, Zhenjiang 212013, China)

Abstract: This study investigates the negative influence of an eccentric permanent-magnet (PM) design on high-frequency electromagnetic vibration in fractional-slot concentrated-winding (FSCW) PM machines. First, an analytical expression for the sideband current harmonics was derived using the double Fourier series expansion method. Then, the characteristics of the flux-density harmonics are studied from the perspective of the space-time distribution and initial phase relationship. The influence of the eccentric PM design on high-frequency electromagnetic and concentrated forces was studied based on the electromagnetic force modulation effect. Consequently, an eccentric PM design is not conducive to reducing the $2p^{th}$-order high-frequency electromagnetic forces. Finally, two FSCW PM machines with conventional and eccentric PM designs are manufactured and tested to verify the theoretical analysis. The results show that the eccentric PM design worsens high-frequency vibrations.

Keywords: Eccentric permanent magnet machine, sideband current harmonics, electromagnetic force modulation effect, fractional-slot concentrated-winding, high-frequency vibration

1 Introduction

Fractional-slot concentrated-winding (FSCW) permanent-magnet (PM) machines are widely used in industrial automation and household appliances because of their high power density and efficiency [1-4]. Additionally, a low-vibration performance is required in these fields [5-7]. Vibrations can be categorized as mechanical and electromagnetic, according to their source. The electromagnetic force acting on the stator teeth is the primary source of electromagnetic vibration. FSCW PM machines have severe vibration problems because of the low spatial order of their electromagnetic forces [8]. Simultaneously, owing to the electromagnetic force modulation effect, the high-order electromagnetic force of the FSCW PM machine must be considered [9-12].

However, research on the high-frequency vibrations of FSCW PM machines is insufficient. With the

progress in power electronics technology, integrated circuit technology, and modern control theory, voltage source inverters using the space vector pulse width modulation (SVPWM) technique are widely used to drive machines to achieve high performance. However, the SVPWM technique generates undesirable sideband harmonics during intrinsic switching, whose frequency is close to the carrier frequency [13]. The high-frequency armature reaction magnetic field components caused by these sideband harmonics interact with other magnetic field components in the air gap, resulting in high-frequency vibration [14]. Therefore, reducing the high-frequency vibrations in FSCW PM machines is of great significance.

Recently, several studies have been conducted on high-frequency vibrations. Analytical expressions of sideband current harmonics were studied using the double Fourier series expansion method [15]. Based on this, analytical approaches for sideband vibrations in integer-slot and fractional-slot machines have been derived [16-17]. Research on high-frequency vibrations should focus on methods for reducing these vibrations. Many methods for reducing sideband current harmonics have been reported in the literature, such as random pulse position [18], random switching

frequency [19], carrier phase shift [20], and variable switching sequences [21]. However, these methods are mainly from the perspective of a control strategy, which increases the difficulty of control. An accurate equivalent circuit for induction machines with auxiliary winding was proposed in Ref. [22] to reduce high-frequency vibrations. However, the number of turns of the stator primary and auxiliary windings is the same, which leads to the auxiliary winding occupying a large slot area. In Ref. [23], the effect of an eccentric PM design on the high-frequency vibration performance of integer-slot PM machines was investigated. It was revealed that high-frequency vibrations could be decreased by reducing the harmonic content of the PM flux density. However, the influence of the eccentric PM design on the high-frequency vibration performance of FSCW PM machines has not been studied.

The remainder of this paper is organized as follows: In Section 2, the models and parameters of the two 12-slot/10-pole FSCW PM machines are presented. In Section 3, analytical expressions for the sideband voltage and current harmonics near the first carrier frequency are derived. In Section 4, the characteristics of PM flux-density harmonics and high-frequency armature reaction flux-density harmonics are studied. In particular, the initial phase relationship of the flux-density harmonics is revealed. In Section 5, the high-frequency electromagnetic force density is derived from Maxwell's tensor equation. Considering the electromagnetic force modulation effect, the influence of the eccentric PM design on the high-frequency electromagnetic and concentrated forces was studied. In Section 6, two FSCW PM machines are tested to verify the deterioration effect of the eccentric PM design on high-frequency vibrations. Finally, the conclusions of this study are presented in Section 7.

2 Prototype machines

To investigate the effect of the eccentric PM design on the high-frequency vibration performance of FSCW PM machines, two 12-slot/10-pole PM machines were designed for analysis. The flux distributions and structures of the two PM machines under no-load conditions are shown in Fig. 1. The primary parameters are listed in Tab. 1. Due to the reduced use of PMs, the pth-order operating harmonic of the eccentric PM machine is less than that of conventional PM machine when the same PM material is used in both conventional and eccentric PM machines. To maintain the pth-order operating harmonics the same for a fair comparison, the remanence of the eccentric PM machine was higher than that of the conventional machine.
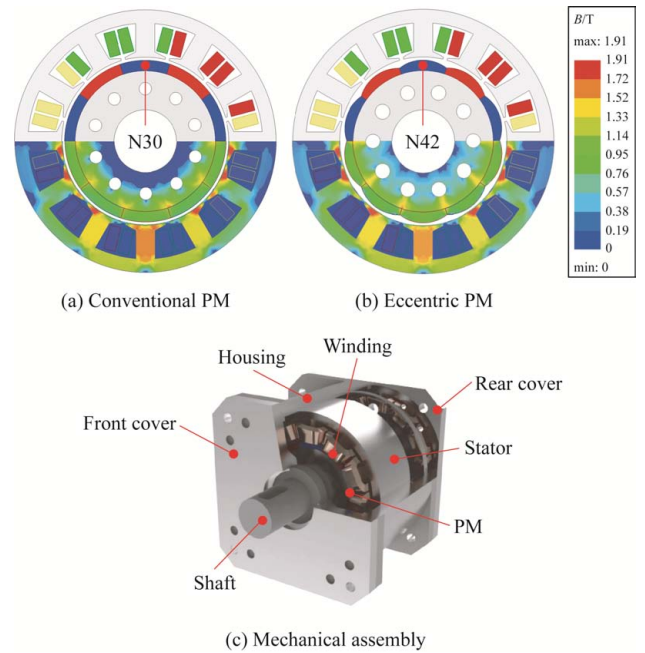

(a) Conventional PM   (b) Eccentric PM

(c) Mechanical assembly

Fig. 1   Flux distribution and structure

Tab. 1   Main parameters of two 12-slot/10-pole FSCW PM machines

Parameters	Conventional	Eccentric
Stator outer diameter/mm	125	125
Stator inner diameter/mm	80	80
Core stack length/mm	50	50
Air gap length/mm	1	1
PM thickness/mm	5	5
Pole embrace	1	1
PM flux linkage/Wb	0.084	0.084
Rated speed/(r/min)	600	600
DC-link voltage/V	100	100
Carrier frequency/kHz	10	10
D-axis inductance/mH	1.62	1.59
Q-axis inductance/mH	1.62	1.59
PM materials	N30	N42
Eccentricity/mm	0	20

3 Sideband current harmonics analysis

The SVPWM technique is widely used in PM machine control strategies. However, SVPWM typically operates at a fixed switching frequency, concentrating the spectrum near the carrier frequency and its multiples. An equivalent modulation process should be established to analyze the harmonics generated by the SVPWM technique. Included in the modulation model are a saddle modulation wave and a triangular carrier wave, which is considered triangular for simplicity. The modulation wave is equivalent to a standard sine wave plus a third harmonic. Ignoring the higher harmonics, the modulation wave $y(t)$ can be approximated as

$$y(t) \approx \frac{2M}{\sqrt{3}}\sin(\omega_e t) + \frac{3M}{4\pi}\sin(3\omega_e t) \tag{1}$$

where M is the modulation coefficient, which depends on the ratio of the modulation wave amplitude to the carrier wave amplitude; ω_e is the angular frequency of the modulation wave.

The phase voltage was obtained by comparing modulation and carrier waves. The main sideband voltage harmonics in the phase voltage can be approximately calculated as

$$U_{sideband} \approx C_{12}\cos\left[(\omega_c \pm 2\omega_e)t\right] + C_{14}\cos\left[(\omega_c \pm 4\omega_e)t\right] \tag{2}$$

$$\begin{cases} C_{12} = \dfrac{2U_{dc}}{\pi}\left[J_2\left(\dfrac{M\pi}{2}\right)J_0\left(\dfrac{3\sqrt{3}M}{16}\right) - J_1\left(\dfrac{M\pi}{2}\right)J_1\left(\dfrac{3\sqrt{3}M}{16}\right)\right] \\ C_{14} = \dfrac{2U_{dc}}{\pi}J_1\left(\dfrac{M\pi}{2}\right)J_1\left(\dfrac{3\sqrt{3}M}{16}\right) \end{cases}$$

where ω_c is the angular frequency of the triangular carrier wave; C_{nm} represents the amplitudes of sideband voltage harmonics with different frequencies. The specific details of C_{nm} are determined by the DC-link voltage and the Bessel function. The frequencies of sideband harmonics can be expressed as $n\omega_c \pm m\omega_e$.

The influence of harmonic permeance and resistance was ignored to simplify the analysis. Through coordinate transformation, the relationship between sideband voltage harmonics and sideband current harmonics can be expressed as

$$\begin{cases} i_{d_\mu} = \dfrac{U_{d_\mu}}{j\omega_\mu L_d} \\ i_{q_\mu} = \dfrac{U_{q_\mu}}{j\omega_\mu L_q} \end{cases} \tag{3}$$

where ω_μ is the angular frequency of the sideband harmonics; L_d and L_q represent the inductance of the d-axis and q-axis, respectively.

The main sideband current harmonics in the phase current can be approximately calculated as

$$i_{sideband} = i_{12}\cos\left[(\omega_c \pm 2\omega_e)t\right] + i_{14}\cos\left[(\omega_c \pm 4\omega_e)t\right] \tag{4}$$

$$\begin{cases} i_{12} = \dfrac{U_{dc}\sqrt{\left(C_{12}^2 + C_{14}^2\right)\left(L_d^2 + L_q^2\right) + 2L_d L_q\left(C_{12}^2 - C_{14}^2\right) + 2C_{12}C_{14}\left(L_d^2 + L_q^2\right)}}{4L_d L_q\left(\omega_c \pm 3\omega_e\right)} \\ i_{14} = \dfrac{U_{dc}\sqrt{\left(C_{12}^2 + C_{14}^2\right)\left(L_d^2 + L_q^2\right) - 2L_d L_q\left(C_{14}^2 - C_{12}^2\right) + 2C_{12}C_{14}\left(L_d^2 + L_q^2\right)}}{4L_d L_q\left(\omega_c \pm 3\omega_e\right)} \end{cases}$$

By analyzing the derivation process of the sideband current harmonics, the amplitudes of the sideband current harmonics were determined by the DC-link voltage, modulation coefficient, and dq-axis inductance. However, the two FSCW PM machines have similar fundamental PM flux linkages and dq-axis inductances. Under the same drive-control system and operating conditions, the eccentric PM design had little effect on the modulation coefficients. Therefore, the sideband current harmonics of the two

FSCW PM machines can be considered identical. Fig. 2 compares the three-phase current waveforms and spectrum analysis of the 12-slot/10-pole FSCW PM machine at 600 r/min. The main sideband current harmonic components near the first carrier frequency include $f_c \pm 2f_e$ and $f_c \pm 4f_e$. The amplitudes of the sideband current harmonics at different rotational speeds are shown in Fig. 3. With an increase in the rotation speed, the amplitudes of the sideband current harmonics near the first carrier frequency gradually
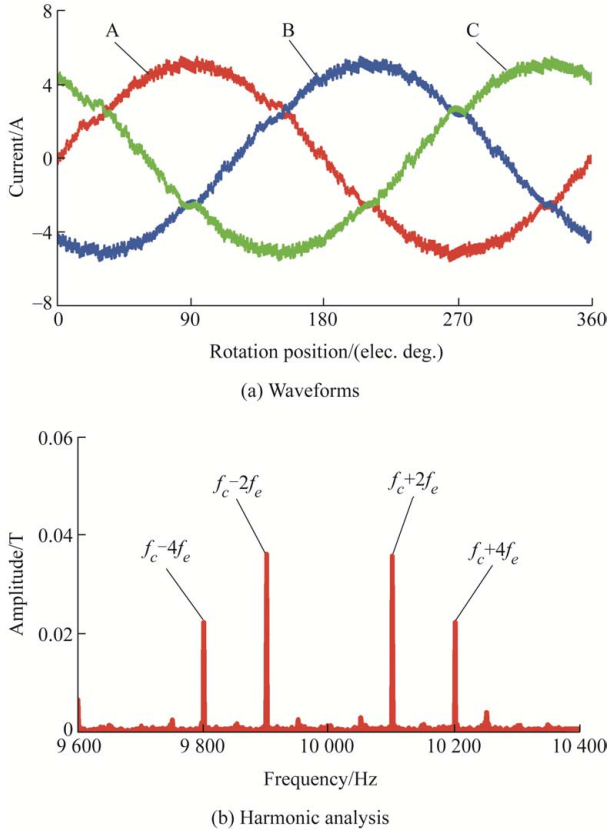
increased.

(a) Waveforms

(b) Harmonic analysis

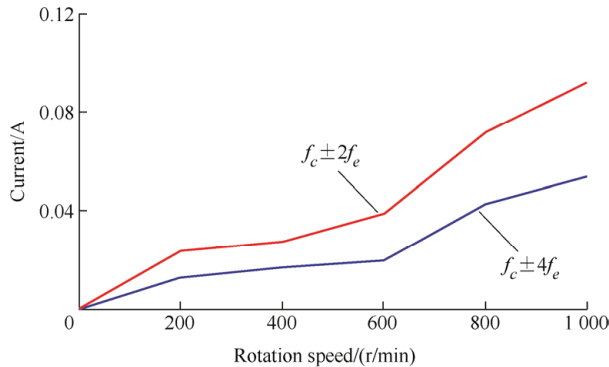Fig. 2   Three-phase current waveforms and spectral analysis

Fig. 3   Sideband current harmonics at different rotation speeds

4   Air-gap flux-density analysis

According to a previous analysis, a PM machine driven by the SVPWM technique inevitably produces sideband current harmonics during operation, generating high-frequency armature reaction fields in the air gap. For high-frequency electromagnetic forces, the main contribution comes from the interaction between the low-frequency PM magnetic field and the high-frequency armature reaction magnetic field. To analyze the properties of the high-frequency electromagnetic force density, it is necessary to

calculate the flux density in the air gap. Generally, the radial and tangential flux-density harmonics have the same spatial and temporal properties, but the amplitudes of the radial components are much larger than those of the tangential components [24]. Therefore, for simplicity, the tangential component is neglected in this study.

4.1   Low-frequency PM flux density

Ignoring the core magnetic reluctance and saturation effects, the PM flux density can be expressed as

$$b_{pm} = \sum_{i}^{\infty} B_{pm} \cos\left(ip\theta - i\omega_e t + \varphi_{pm}\right) \qquad (5)$$

where p is the pole pair of the FSCW PM machine and i is an odd number.

The PM flux-density waveforms of the 12-slot/10-pole FSCW PM machines and the spectrum analysis are shown in Fig. 4. The pth-order harmonic amplitudes of the two PM machines are almost equal. The PM flux-density waveform of the eccentric PM machine has a lower harmonic content than that of the conventional PM machine. In addition, it is clear from spectral analysis that the eccentric PM design reduces
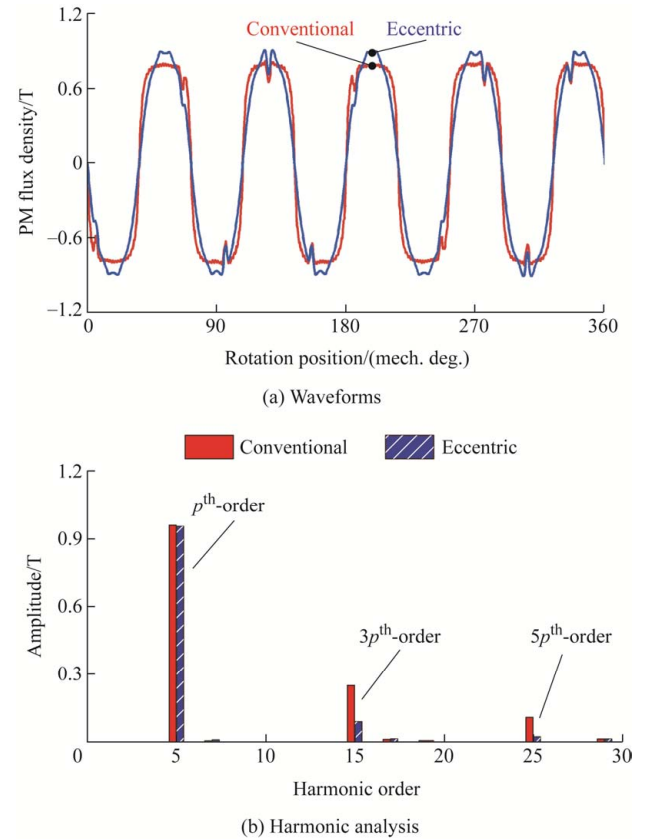

(a) Waveforms

(b) Harmonic analysis

Fig. 4   Comparison of PM flux densities

the $3p$th-order and $5p$th-order PM flux densities. However, because the electromagnetic force harmonics are vectors, phase synthesis or cancellation occurs between the electromagnetic force harmonics of the same temporal and spatial orders [25]. Therefore, the initial phases of the flux-density harmonics must be considered when analyzing electromagnetic force harmonics. Fig. 5 shows the initial phases of PM flux-density harmonics. Although the amplitudes of the main PM flux-density harmonics were quite different, they all had the same initial phases.
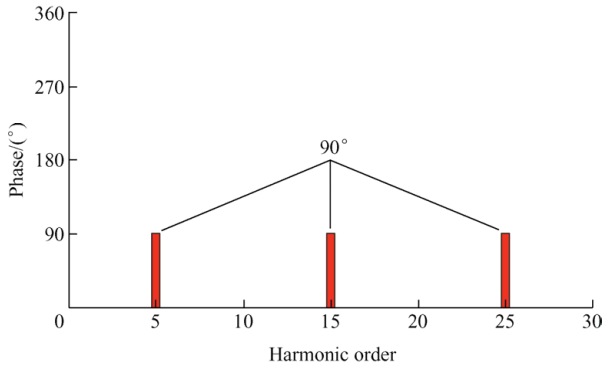

Fig. 5   Initial phases

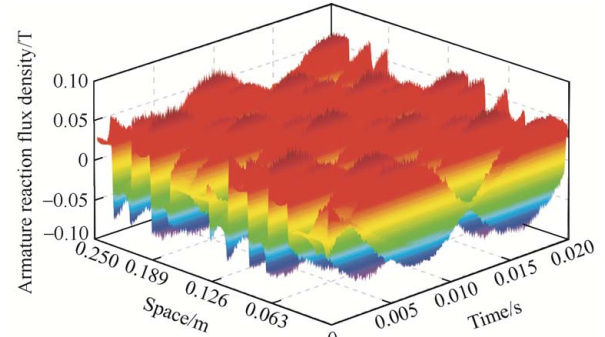## 4.2   High-frequency armature reaction flux density

Based on the analysis of the sideband current harmonics, the high-frequency armature reaction flux density can be expressed as

$$b_{arm\_\mu} = \sum_{v}^{\infty} \sum_{\mu}^{\infty} B_{arm\_\mu} \sin\left[(vN_t + kZ)\theta - \omega_\mu t + \varphi_{arm\_\mu}\right]$$

(6)

where Z is the number of slots; N_t is equal to the greatest common divisor of the pole pair and slot number of the FSCW PM machine; v is an odd number and satisfies $v = 6k \pm 1$, and $k = \pm 1, 2, 3, \cdots$.

As the stator and winding structures of the two FSCW PM machines are the same, the armature reaction magnetic fields can be considered to be the same. Fig. 6a shows that the high-frequency armature reaction flux density exhibits a time-space correlation distribution. Fig. 6b shows the results of temporal and spatial spectral analyses. The frequencies of the high-frequency armature reaction flux-density harmonics are mainly distributed at $f_c \pm 2f_e$ and $f_c \pm 4f_e$, which are the same as those of the sideband current harmonics. Fig. 7 shows the initial phases of the

high-frequency armature reaction flux-density harmonics. There were significant differences in the initial phases of the high-frequency armature reaction flux-density harmonics for different space and time orders.

(a) Waveforms
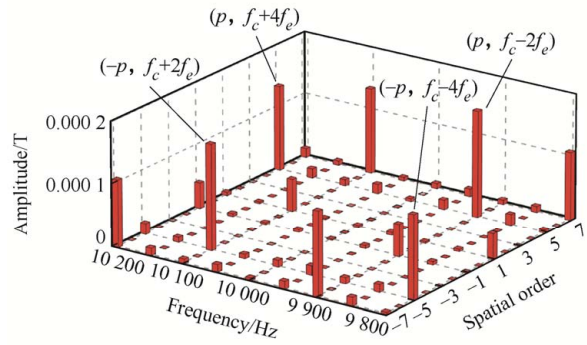
(b) Harmonic analysis
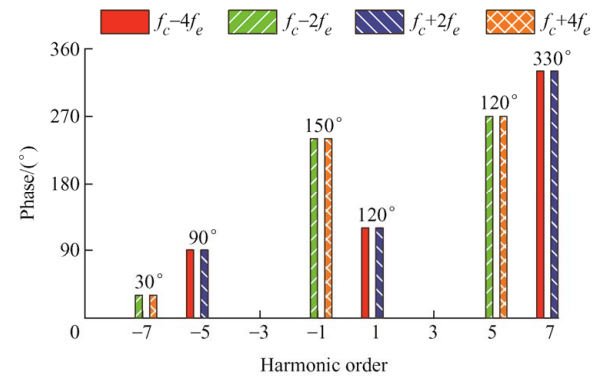
Fig. 6   Armature reaction flux density

Fig. 7   Initial phases

5   High-frequency electromagnetic force analysis

The high-frequency electromagnetic force acting on the stator teeth is the main cause of high-frequency vibrations. In Section 4, the amplitudes and initial phases of the main flux-density harmonics are determined. According to the Maxwell stress tensor equation, the high-frequency electromagnetic force density can be approximated as follows

$$f_r \approx \frac{b_{pm}\, b_{arm\_\mu}}{\mu_0} \qquad (7)$$

where μ_0 is vacuum permeability. Substituting Eq. (7) and Eq. (8) into Eq. (9), the high-frequency electromagnetic force density can be obtained as follows

$$f_r = \sum_{\mu}\sum_{i}\sum_{v} \sigma_r \cos\left[\left(ip \pm vN_t\right)\theta \pm \left(\omega_\mu \pm n\omega_e\right)t + \varphi_\mu\right] \quad(8)$$

5.1 Electromagnetic force modulation effect

In traditional vibration analysis models for PM machines, the stator core is typically equivalent to a cylindrical structure. The vibrational displacement due to electromagnetic force can be calculated using Jordan's formula as follows

$$\begin{cases} Y_{sv}(v = 0) = \dfrac{R_i R_y}{E h_y}\sigma_r \\[2mm] Y_{sv}(v \geqslant 2) = \dfrac{12 R_i R_y^3}{E h_y^3 (v^2 - 1)^2}\sigma_r \\[2mm] Y_{dv} = Y_{sv}\left[(1 - f_v^2 / f_j^2)^2 + 4\xi_j^2 f_v^2 / f_j^2\right]^{-1/2} \end{cases} \quad(9)$$

where Y_{sv} and Y_{dv} are static and dynamic vibration displacements; R_i is the inner radius of the stator; R_y and h_y are the radius and thickness of the stator yoke; E is the elastic modulus; f_j, and ξ_j are the frequency and damping of jth-order mode.

Eq. (9) shows that the low-order electromagnetic force is a critical factor in the vibration of the FSCW PM machines [26]. However, Eq. (9) ignores the electromagnetic force modulation effect due to stator slotting [27]. Higher-order electromagnetic force harmonics can induce significant vibration responses through electromagnetic force modulation effects. The vibration analysis of the FSCW PM machines is biased if only low-order electromagnetic force harmonics are considered.

According to the Nyquist-Shannon sampling theorem, the modulated electromagnetic force density can be expressed as

$$\begin{cases} f_m = \sigma_r \cos(v\theta + \omega_v t + \varphi_v) & v \leqslant \dfrac{Z}{2} \\[2mm] f_m = \sigma_r \cos\left[(v - kZ)\theta + \omega_v t + \varphi_v\right] & v > \dfrac{Z}{2} \end{cases} \quad(10)$$

where f_m is the modulated electromagnetic force density, and σ_r, ω_v, and φ_v are the amplitude, angular velocity, and initial phase of the vth-order modulated electromagnetic force density. When the spatial order v is greater than $Z/2$, electromagnetic force modulation will occur. For the 12-slot/10-pole FSCW PM machine, the $2p$th-order high-frequency electromagnetic force density has a high amplitude and can be modulated into a low-order high-frequency electromagnetic force with a high amplitude. Fig. 8 shows a schematic of the electromagnetic force modulation effect. The $2p$th-order electromagnetic force was modulated into 2nd-order by the 12 stator teeth, affecting the high-frequency vibration performance.
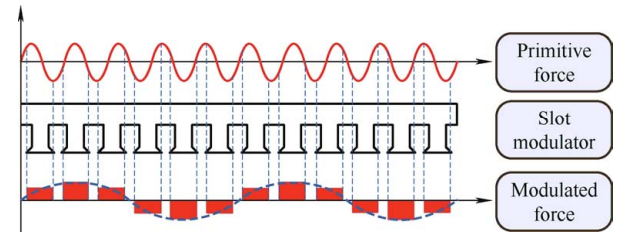

Fig. 8   Electromagnetic force modulation

The interaction between the low-frequency PM flux density and high-frequency armature reaction flux density mainly generates a $2p$th-order high-frequency electromagnetic force density. The spatial order, frequency, and initial phases of the $2p$th-order high-frequency electromagnetic force density can be derived as shown in Tab. 2.

Tab. 2 $2p$th-order high-frequency electromagnetic force density

PM flux density	Armature reaction flux density	Electromagnetic force density
$(p, f_e, 90°)$	$(p, f_c - 2f_e, 270°)$	$(2p, f_c - f_e, 0)$
$(3p, 3f_e, 90°)$	$(-p, f_c - 4f_e, 90°)$	$(2p, f_c - f_e, 180°)$
$(p, f_e, 90°)$	$(p, f_c + 4f_e, 270°)$	$(2p, f_c + 5f_e, 0)$
$(3p, 3f_e, 90°)$	$(-p, f_c + 2f_e, 90°)$	$(2p, f_c + 5f_e, 180°)$
$(3p, 3f_e, 90°)$	$(p, f_c - 2f_e, 270°)$	$(-2p, f_c - 5f_e, 180°)$
$(p, f_e, 90°)$	$(-p, f_c - 4f_e, 90°)$	$(-2p, f_c - 5f_e, 0)$
$(3p, 3f_e, 90°)$	$(p, f_c + 4f_e, 270°)$	$(-2p, f_c + f_e, 180°)$
$(p, f_e, 90°)$	$(-p, f_c + 2f_e, 90°)$	$(-2p, f_c + f_e, 0)$

It can be seen that the $2p$th-order high-frequency electromagnetic force density generated by the pth-order PM flux density is opposite to that generated by the $3p$th-order PM flux density. Consequently, this means that the $2p$th-order high-frequency electromagnetic force density generated by the $3p$th-order PM flux density decreases the total

Jinghua Ji et al.: Investigation of Eccentric PM on High-frequency Vibration in FSCW PM Machine
Considering Force Modulation Effect

65

amplitude of the $2p^{th}$-order high-frequency electromagnetic force density.

The spatial order and corresponding frequency characteristics of the high-frequency electromagnetic force density harmonics near the first carrier frequency were derived using two-dimensional Fourier decomposition, as shown in Fig. 9.
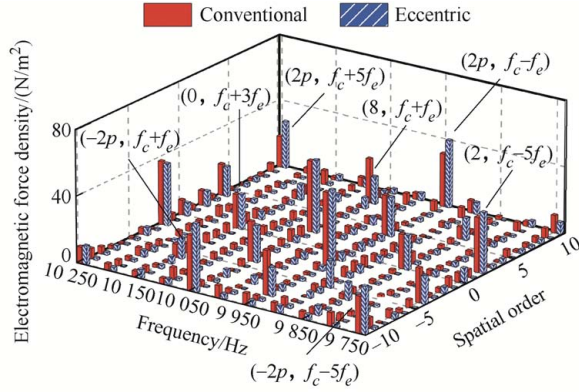

Fig. 9   Comparison of high-frequency electromagnetic force densities

The high-frequency electromagnetic force density harmonics with large amplitudes were mainly 0th-order, 2nd-order, and $2p^{th}$-order. However, because the pth-order operating harmonics of the two PM machines were almost equal, the 0th-order and 2nd-order high-frequency electromagnetic force density harmonics were almost the same. Eccentric PM machines reduce the $3p^{th}$-order PM flux density, thereby significantly reducing the amplitude of the 8th-order high-frequency electromagnetic force density. However, the spatial order of the 8th-order electromagnetic force density was large and had a limited effect on high-frequency vibrations. The most remarkable feature was that the $2p^{th}$-order high-frequency electromagnetic force density of the conventional PM machine was lower than that of the eccentric PM machine. The FSCW PM machine with an eccentric PM was verified to have a negative effect on the reduction of the $2p^{th}$-order high-frequency electromagnetic force density.

5.2   Concentrated force computation

According to the force transformation model, the force distributed on the tooth surface can be converted into a concentrated force and moment. Fig. 10 shows the transfer model from the force density to the concentrated force.
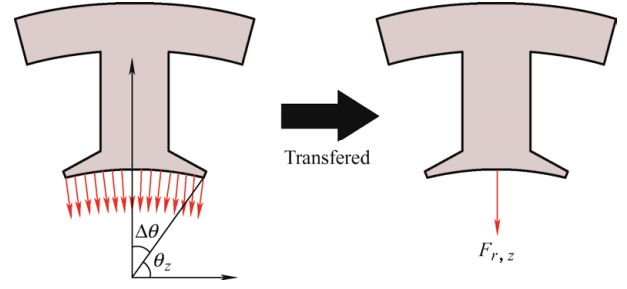

Fig. 10   Concentrated force transformation

Ignoring the tangential force, the expressions for the radial concentrated force can be simplified to

$$F_{r,z} = L_s R_{is} \int_{\theta_z - \Delta\theta}^{\theta_z + \Delta\theta} f_{\eta\_r} \cos(\theta_z - \theta)\mathrm{d}\theta \tag{11}$$

where L_s is the effective length; R_{is} is the armature diameter; θ_z is the angle of the tooth, and $\Delta\theta$ is the half of the tooth surface angle.

Fig. 11 shows the spectral results for the concentrated force transferred from the high-frequency electromagnetic force density near the first carrier frequency. The $2p^{th}$-order high-frequency electromagnetic force density was modulated to a 2nd-order concentrated force.
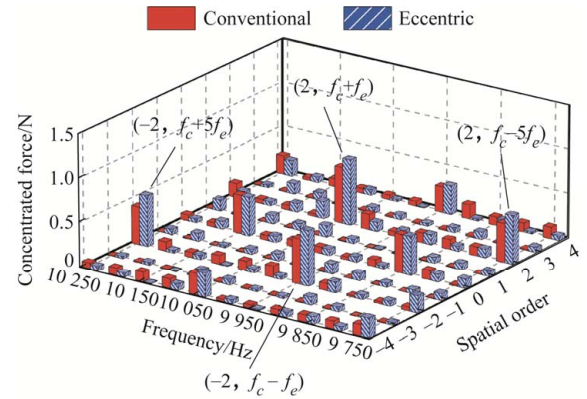

Fig. 11   Comparison of concentrated forces

6   Experimental validation

6.1   Modal parameters

Fig. 12 shows the prototypes of the two 12-slot/10-pole FSCW PM machines. The modal tests of the stator, stator with coils, and the entire machine are shown in Fig. 13. The two PM machines differed

only in the shape of the PM; therefore, the modal parameters of the two prototypes were essentially identical. To avoid repetition, the modal tests were performed using only one prototype. The prototype was suspended from an elastic rope to simulate free constraints. Acceleration sensors were mounted on the housing to obtain acceleration data. Vibration acceleration data were obtained by hammering the prototype, and frequency response function curves were obtained. The modal parameters, including the mode shapes, frequencies, and damping ratios, were automatically generated using the software, and are listed in Tab. 3. The anisotropic material parameters of the stator core, windings, and housing are listed in Tab. 4.
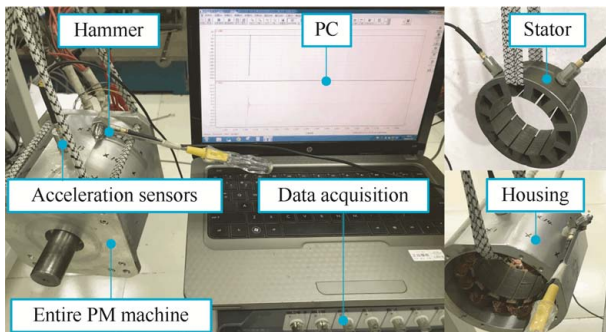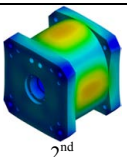

(a) Stator   (b) Conventional PM   (c) Eccentric PM
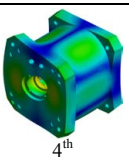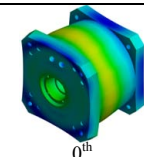
Fig. 12   12-slot/10-pole FSCW PM machine
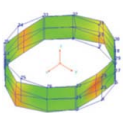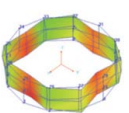
Fig. 13   Modal test

Tab. 3   Modal parameters

Parameter	Value		
Simulated shape	2nd	4th	0th
Simulated frequency/Hz	3 080.3	7 371.4	10 450.9
Tested shape			—
Tested frequency/Hz	3 084.1	7 393.2	—
Errors(%)	0.12	0.29	—
Damping ratio (%)	0.91	2.17	1.72

Tab. 4   Equivalent material parameters

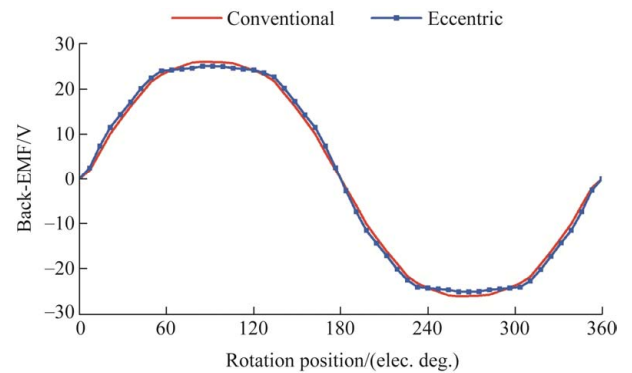| Items	Symbol	Stator core	Windings	Housing
Density/(kg/m³)	ρ	7 860	5 822	2 770
Young's modulus/GPa	E_x	205	0.2	
	E_y	205	0.2	70
	E_z	170	1	
Shear modulus/GPa	G_{xy}	55	0.1	
	G_{yz}	26.5	0.14	25.6
	G_{xz}	26.5	0.14	
Poisson's ratio	u_{xy}	0.3	0.2	
	u_{yz}	0.27	0.1	0.33
	u_{xz}	0.27	0.1	

6.2   Vibration response

Fig. 14a shows the back-EMF waveforms of the 12-slot/10-pole FSCW PM machines with conventional and eccentric PM designs at 600 r/min. Fig. 14b shows the results of the corresponding spectral analyses. The back-EMF harmonic content of the eccentric PM machine is lower than that of the conventional PM machine.


(a) Waveforms
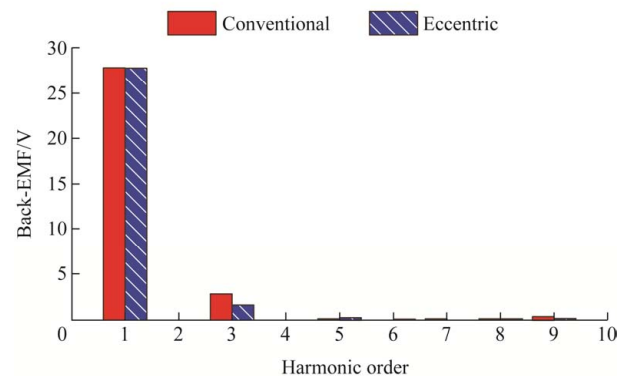
(b) Harmonic analysis

Fig. 14   Comparison of back EMF

Jinghua Ji et al.: Investigation of Eccentric PM on High-frequency Vibration in FSCW PM Machine
Considering Force Modulation Effect

67

Fig. 15 shows the two experimental platforms used for PM machine vibration testing. The acceleration transducer was set to 32 kHz to acquire test data around the first carrier frequency. A dynamic signal acquisition instrument was used to acquire the vibration test data from the transducer, and a programmable DC signal source from Chroma provided the DC bus voltage. The digital signal processor, DSP TMSS20F28377, executes the SVPWM control algorithm.
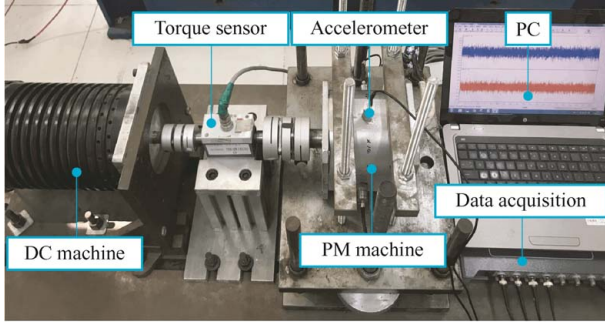
(a) Vibration test platform
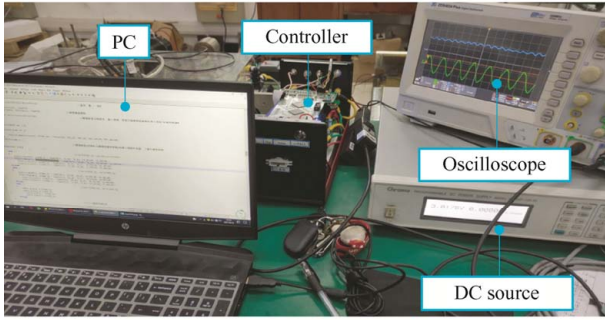
(b) Setup of drive and control systems

Fig. 15   Experimental test platform

Figs. 16a and 16b compare the high-frequency vibration accelerations measured by the two 12-slot/10-pole FSCW PM machines under no-load conditions at 600 r/min and 1 200 r/min, respectively. As mentioned above, the eccentric PM design increases the amplitude of the $2p^{th}$-order high-frequency electromagnetic force density. The vibration acceleration of the eccentric PM machine is significantly higher at $f_c \pm f_e$ and $f_c \pm 5f_e$ compared to the conventional PM machine. Fig. 16c compares the high-frequency vibration accelerations measured for the two 12-slot/10-pole FSCW PM machines under load conditions of 600 r/min. The high-frequency vibration acceleration under the loaded condition was slightly higher than that under the no-load condition.

(a) No load at 600 r/min

(b) No load at 1 200 r/min

(c) Load at 600 r/min
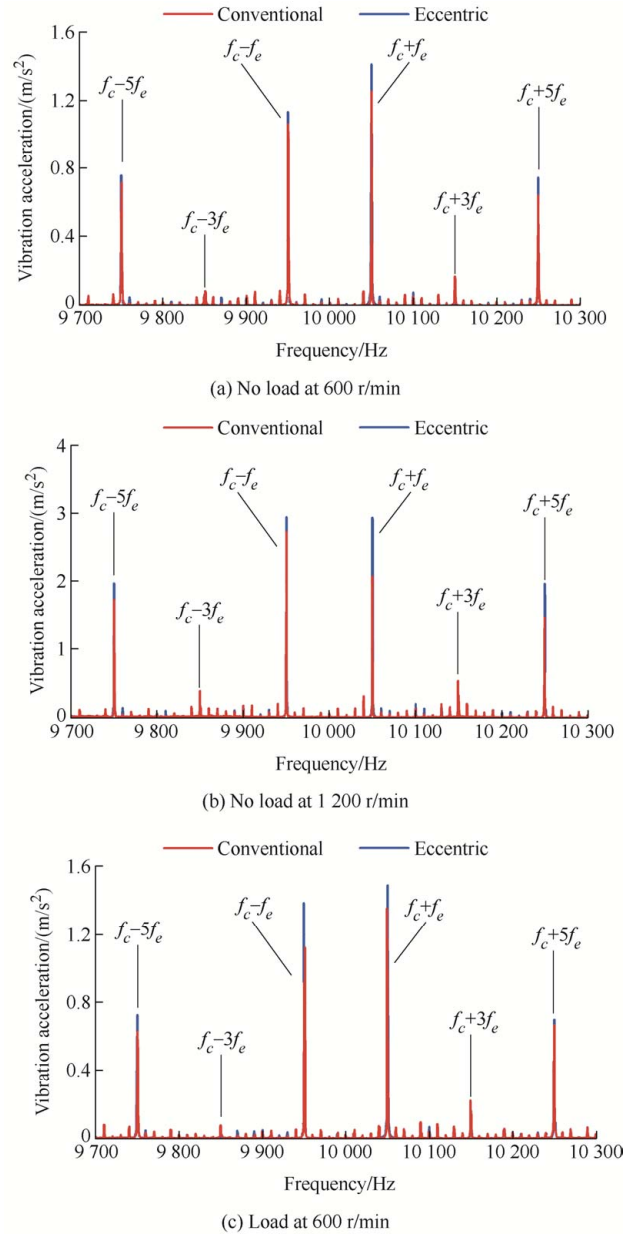
Fig. 16   Comparison of vibration accelerations

7   Conclusions

In this study, the negative effects of an eccentric PM design on the high-frequency electromagnetic force and vibrations of an FSCW PM machine were investigated. The analytical expression of the sideband current harmonics generated by SVPWM technology was derived. Then, the temporal and spatial distributions and initial phase relationship of the low-frequency PM flux-density harmonics and high-frequency armature reaction flux-density harmonics were clarified. The eccentric PM design weakens the $3p^{th}$-order PM flux-density harmonic. However, the initial phase of the $2p^{th}$-order

high-frequency electromagnetic force generated by the $3p^{th}$-order PM flux density was opposite to that generated by the pth-order PM flux density. The eccentric PM design has a negative impact on the reduction in the total $2p^{th}$-order high-frequency electromagnetic force. Finally, two 12-slot/10-pole FSCW PM machines were manufactured and experimental vibration results were used to verify the theoretical analysis.

References

[1] F Yan, J Ji, Z Ling, et al. Magnets shifting design of dual PM excited vernier machine for high-torque application. *Chinese Journal of Electrical Engineering*, 2022, 8(3): 90-101.

[2] X Chen, J Wang. Magnetomotive force harmonic reduction techniques for fractional-slot non-overlapping winding configurations in permanent-magnet synchronous machines. *Chinese Journal of Electrical Engineering*, 2017, 3(2): 102-113.

[3] E Carraro, N Bianchi, S Zhang, et al. Design and performance comparison of fractional slot concentrated winding spoke type synchronous motors with different slot-pole combinations. *IEEE Transactions on Industry Applications*, 2018, 54(3): 2276-2284.

[4] R Dutta, A Pouramin, M F Rahman. A novel rotor topology for high-performance fractional slot concentrated winding interior permanent magnet machine. *IEEE Transactions on Energy Conversion*, 2021, 36(2): 658-670.

[5] Z Li, J Xia, Z Guo, et al. Analysis and reduction of pole-frequency vibration of surface mounted permanent magnet synchronous machines with fractional slot concentrated winding considering the radial and tangential forces. *IEEE Transactions on Transportation Electrification*, 2023, 9(2): 2129-2140.

[6] Z Wu, Y Fan, C H T Lee, et al. Vibration optimization of FSCW-IPM motor based on iron-core modification for electric vehicles. *IEEE Transactions on Vehicular Technology*, 2020, 69(12): 14834-14845.

[7] S Das, A Chowdhury, Y Sozer, et al. Sensitivity analysis based NVH optimization in permanent magnet synchronous machines using lumped unit force response. *IEEE Transactions on Industry Applications*, 2022, 58(3): 3533-3544.

[8] S Zhu, W Zhao, J Ji, et al. Design to reduce modulated vibration in fractional-slot concentrated-windings PM machines considering slot-pole combination. *IEEE Transactions on Transportation Electrification*, 2023, 9(1): 575-585.

[9] W Zhao, Q He, W Tian, et al. Investigation of winding configuration on electromagnetic vibration in modular dual three-phase PM machine. *IEEE Transactions on Industrial Electronics*, 2024, 71(2): 1257-1267.

[10] H Fang, D Li, R Qu, et al. Modulation effect of slotted structure on vibration response in electrical machines. *IEEE Transactions on Industrial Electronics*, 2019, 66(4): 2998-3007.

[11] S Wang, J Hong, Y Sun, et al. Analysis of zeroth-mode slot frequency vibration of integer slot permanent-magnet synchronous motors. *IEEE Transactions on Industrial Electronics*, 2020, 67(4): 2954-2964.

[12] S Zhu, W Zhao, J Ji, et al. Investigation of bread-loaf magnet on vibration performance in FSCW PMSM considering force modulation effect. *IEEE Transactions on Transportation Electrification*, 2021, 7(3): 1379-1389.

[13] D G Holmes, T A Lipo. Modulation of three-phase voltage source inverters, in pulse width modulation for power converters: Principles and practice. 5th ed. NJ: Wiley, 2003.

[14] Z Qiu, Y Chen, X Liu, et al. Analysis of the sideband current harmonics and vibro-acoustics in the PMSM with SVPWM. *IET Power Electronics*, 2020, 13(5): 1033-1040.

[15] W Liang, J Wang, P C-K Luk, et al. Analytical modeling of current harmonic components in PMSM drive with voltage-source inverter by SVPWM technique. *IEEE Transactions on Energy Conversion*, 2014, 29(3): 673-680.

[16] W Liang, P C-K Luk, W Fei. Analytical investigation of sideband electromagnetic vibration in integral-slot PMSM drive with SVPWM technique. *IEEE Transactions on Power Electronics*, 2017, 32(6): 4785-4795.

[17] W Liang, P C-K Luk, W Fei. Investigation of magnetic field interharmonics and sideband vibration in the FSCW IPMSM drive with the SPWM technique. *IEEE Transactions on Power Electronics*, 2018, 33(4): 3315-3324.

[18] W Deng, J Huang, Z Qian, et al. A random pulse position-based selective noise cancellation modulation

Jinghua Ji et al.: Investigation of Eccentric PM on High-frequency Vibration in FSCW PM Machine
Considering Force Modulation Effect

69

method for SVPWM driven PMSMs. *IEEE Transactions on Energy Conversion*, 2022, 37(3): 2190-2198.

[19] F Bu, Q Liu, T Pu, et al. Analysis and performance of five-phase piecewise-random-switching-frequency space vector pulse width modulation. *IEEE Transactions on Energy Conversion*, 2021, 36(3): 2339-2347.

[20] X Han, D Jiang, T Zou, et al. Two-segment three-phase PMSM drive with carrier phase-shift PWM for torque ripple and vibration reduction. *IEEE Transactions on Power Electronics*, 2019, 34(1): 588-599.

[21] D Ye, J Li, R Qu, et al. Variable switching sequence PWM strategy of dual three-phase machine drive for high-frequency current harmonic suppression. *IEEE Transactions on Power Electronics*, 2020, 35(5): 4984-4995.

[22] S Xia, S Wang. Reduction of switching frequency vibration of induction machines by auxiliary winding with capacitors. *IEEE Transactions on Energy Conversion*, 2022, 37(1): 367-376.

[23] T Liu, W Zhao, J Ji, et al. Effects of eccentric magnet on high-frequency vibroacoustic performance in integral-slot SPM machines. *IEEE Transactions on Energy Conversion*, 2021, 36(3): 2393-2403.

[24] S Zuo, F Lin, X Wu. Noise analysis, calculation, and reduction of external rotor permanent-magnet synchronous motor. *IEEE Transactions on Industrial Electronics*, 2015, 62(10): 6204-6212.

[25] W Zhao, S Zhu, J Ji, et al. Analysis and reduction of electromagnetic vibration in fractional-slot concentrated-windings PM machines. *IEEE Transactions on Industrial Electronics*, 2022, 69(4): 3357-3367.

[26] J Ji, D Liu, Y Zeng, et al. Vibration reduction and torque improvement of integral-slot SPM machines using PM harmonic injection. *Chinese Journal of Electrical Engineering*, 2023, 9(4): 41-53.

[27] Y Zhou, J Ji, W Zhao, et al. Modulated vibration reduction design for integral-slot interior permanent magnet synchronous machines. *IEEE Transactions on Industrial Electronics*, 2022, 69(12): 12249-12260.

Jinghua Ji received the B.Sc., M.Sc., and Ph.D. degrees in Electrical Engineering from Jiangsu University, Zhenjiang, China, in 2000, 2003, and 2009, respectively.

Since 2000, she has been with the School of Electrical and Information Engineering, Jiangsu University, where she is currently a Professor. From 2013 to 2014, she was a Visiting Scholar with the Department of Electronic and Electrical Engineering, University of Sheffield, Sheffield, UK. She has authored or coauthored over 50 technical papers in these areas. Her research interests include electrical machines and motor drives.

Weizhi Jiang received the B.Sc. degree in Electrical Engineering from Southeast University Cheng Xian College, Nanjing, China, in 2021. He is currently working toward the M.Sc. degree in Electrical Engineering at Jiangsu University.

His current research interests include electromagnetic design and vibration calculation of PMSM systems.

Wenxiang Zhao (M'08-SM'14) received the B.Sc. and M.Sc. degrees in Electrical Engineering from Jiangsu University, Zhenjiang, China, in 1999 and 2003, respectively, and the Ph.D. degree in Electrical Engineering from Southeast University, Nanjing, China, in 2010.

From 2008 to 2009, he was a Research Assistant with the Department of Electrical and Electronic Engineering, University of Hong Kong, Hong Kong, China. From 2013 to 2014, he was a Visiting Professor with the Department of Electronic and Electrical Engineering, University of Sheffield, Sheffield, UK. Currently, he is a Professor with the School of Electric Power Engineering, Nanjing Institute of Technology, and also with School of Electrical and Information Engineering, Jiangsu University. He has authored and coauthored over 150 papers published in various IEEE TRANSACTIONS. His current research interests include electric machines and control.

Tong Liu received the B.Sc. degree in Electrical Engineering from Jiangsu University, Zhenjiang, China, in 2018. He is currently working toward the Ph.D. degree in Electrical Engineering at Jiangsu University.

His current research interests include modeling and calculation of electromagnetic force, vibration, and acoustic noise of PMSM systems.